journal

J. Am. Ceram. Soc., 1–6 (2016)
DOI: 10.1111/jace.14188

Structure and Luminescence in Long Persistence Eu, Dy, and B Codoped Strontium Aluminate Phosphors: The Boron Effect

Guliz Inan Akmehmet,[‡] Sašo Šturm,[§] Laura Bocher,[¶] Mathieu Kociak,[¶] Bojan Ambrožič,[§] and Cleva W. Ow-Yang[*,‡,‖,†]

[‡]Materials Science and Engineering Program, Sabanci University, Orhanli, Tuzla, Istanbul 34956, Turkey

[§]Department of Nanostructured Materials, Jožef Stefan Institute, Jamova Cesta 39, Ljubljana 1000, Slovenia

[¶]Laboratoire de Physique des Solides, Bâtiment 510, CNRS UMR 8502, Université Paris-Sud XI, Orsay F-91405, France

[‖]Nanotechnology Research and Application Center, Sabanci University, Orhanli, Tuzla, Istanbul 34956, Turkey

Long persistence phosphors are promising materials for energy-saving applications, due to their ability to temporarily store and release light. While boron is known to dramatically extend the afterglow persistence to longer than 8 h in strontium aluminates, previous attempts to understand the role of boron neglected any nanoscale-related effects and have been inconclusive. Herein, nanoscale-resolved cathodoluminescence mapping is correlated with selected area electron diffraction and with energy dispersive x-ray spectroscopy analysis using a 2 Å-diameter probe. The salient aspect of this unique approach is that one can not only determine the elemental distribution in the phosphor microstructure, but more importantly, one can discriminate between the distributions of different divalent and trivalent luminescing ions. We demonstrate that the extremely long afterglow is due to the boron dopant via two key roles: (1) facilitating dominance of the long persistence phase during the microstructural evolution and (2) promoting more uniform distribution of the optically active, Eu^{2+} ion in the Sr^{2+} cation sublattice.

I. Introduction

With an impressive capacity for the temporary storage and slow release of light, long afterglow phosphors are very attractive for applications emphasizing energy efficiency. Among these, strontium aluminates show high quantum efficiency when doped with Eu^{2+} and increased persistence duration when additionally doped with Dy^{3+}.[1–3] The strontium aluminates serve as stable hosts in five different primary phases: $SrAl_2O_4$ (SA), $SrAl_4O_7$ (SA_2), $SrAl_{12}O_{19}$ (SA_6), $Sr_3Al_2O_6$ (S_3A), and $Sr_4Al_{14}O_{25}$ [$(SrO)_4{\cdot}(Al_2O_3)_7$, or S_4A_7]—although only SA and S_4A_7 are associated with an extended afterglow. Each phase consists of chains of charged (AlO_x) polyhedra forming a scaffold and defining cavities of negative charge, into which Sr^{2+} ions are incorporated to provide electrical charge neutrality.[4] Eu^{2+} ions are the optically active centers, emitting visible luminescence upon relaxation from $4f^65d^1$ to $4f^7$ levels.[1] These ions enter the crystal structure by substituting into Sr^{2+} ion sites,[5,6] and the consequent differences in crystal field splitting result in distinguishable radiative relaxations.[1,4] Because the orbitals of Eu^{2+} are highly sensitive to even subtle changes in the crystal field,[7–9] the features in the emission spectra can reveal different environments of Eu dopants in crystal lattices. For example, in the crystal structure of (S_4A_7), there are two, equally abundant, crystallographically nonequivalent Sr^{2+} sites—a higher symmetry site and a lower symmetry site. In addition, the codopant Dy^{3+} ions situated in close proximity to the Eu^{2+} offers trap levels near the $4f^65d^1$ level, allowing trapping of the excited electronic charges, which are easily susceptible to thermally stimulated release.[3,4,10] This thermally stimulated de-trapping is associated with extending the afterglow duration of Eu-doped strontium aluminate compounds.[3,5,11]

During ceramic processing by solid-state reaction, B_2O_3 is commonly added as a sintering flux agent. In the case of strontium aluminate compounds, the dramatic extension of afterglow persistence was observed as a serendipitous side effect of the addition of B, from tens of minutes to longer than 14 h.[12–14] To explain the effect of boron, many different theories have been proposed, but no consensus has been reached in the phosphor materials community due to the lack of direct experimental evidence.[10] The most convincing computational model proposed suggests that the answer may lie in the aggregation of ionic defects: the substitutional rare-earth dopants, oxygen vacancies, and B point defects.[5,15–17] Such a model necessitates the positioning of point defects of sufficient proximity for direct energy transfer between electronic trap levels.[5,18–21] The nonuniform distribution of ionic defects is thus presumed to enable persistent luminescence.

To elucidate the impact of boron on the distribution and electronic structure of ionic defects, we systematically investigated the correlation at the nanoscale between structure and optical properties in long persistence S_4A_7ED phosphor compounds with and without B doping. For the ceramic phosphor synthesis, we used a modified sol–gel Pechini process,[22,23] which allows better control over the phase purity and which would thus enable detailed analysis of electronic states within the electronic structure of a single crystal. The globally averaged elemental stoichiometry, phase composition, and optical properties were analyzed to compare the performance of our synthesized product with that reported in the literature. The cornerstone of our methodology involves correlating the local phase composition, optical properties, and elemental stoichiometry at nanoscale resolution by using selected-area electron-diffraction (SADP) analysis, cathodoluminescence (nano-CL), and energy dispersive x-ray spectroscopy (EDXS) analysis using a 2 Å-diameter probe.

II. Experimental Procedure

$Sr_4Al_{14}O_{25}$ phosphor compounds were synthesized by a modified Pechini sol–gel method based on nitrate precursors

C.W. Ow-Yang—contributing editor

Manuscript No. xxxxx. Received August 20, 2015; approved January 28, 2016.
*Member, The American Ceramic Society.
[†]Author to whom correspondence should be addressed. e-mail: cleva@sabanciuniv.edu

—aluminum nitrate nonahydrate [$Al(NO_3)_3{\cdot}9H_2O$], strontium nitrate anhydrous [$Sr(NO_3)_2$], europium nitrate hexahydrate [$Eu(NO_3)_3{\cdot}6H_2O$], dysprosium nitrate pentahydrate [$Dy(NO_3)_3{\cdot}5H_2O$]—and boron oxide (B_2O_3), the chelating agent, citric acid monohydrate ($C_6H_8O_7$), and the gelling agent ethylene glycol ($C_2H_6O_2$). These precursors were added to boiling water in the order listed. For B doping, B_2O_3 was added in amounts of 10, 20, and 30 at.% (starting material mass has an error 81 ± 1 mg). The mixture produced was then subjected to a three-stage thermal treatment: (i) drying of the sol–gel, (ii) calcination, and (iii) reduction in Eu^{3+} via $Eu^{3+} \rightarrow Eu^{2+} + e'$.

The sol–gel mixture was dried in a muffle furnace for 24 h at *ca.* 383 K, yielding a foam-like substance. To determine the heat-treatment procedure of this amorphous precursor, we performed thermogravimetric-differential thermal analysis (TG-DTA) on a specimen containing no boron. The TG-DTA (Netzsch STA 449C Jupiter, Selb, Germany) measurements were conducted dry nitrogen gas (99.99% purity) environments. The following thermal treatment procedure was determined:

1. The dried amorphous mixture was heat-treated at 873 K in air for 6 h to burn off the organic moieties.
2. The furnace temperature was subsequently increased to 1423 K for 10 h of calcination in an ambient air atmosphere.
3. After 10 h at 1423 K, the product was quenched to room temperature.
4. Eu^{3+} was reduced to Eu^{2+} at 1423 K for 3 h under a varigon atmosphere (96% Ar, 4% H_2) and allowed to cool to room temperature in the furnace. The 3-h reduction time was determined to be the optimal duration for balancing the concentration of optically active Eu^{2+} against oxygen vacancy concentration in the host crystal lattice.

To investigate the effect of B on the crystalline compound formation, TG-DTA was performed on all B-doped compositions. Dynamic analysis enabled us to compare the crystallization onset, whereas isothermal analysis allowed us to determine the duration of crystallization at 1423 K. Elemental stoichiometry of the ceramic powders produced was analyzed in inductively coupled plasma by using optical emission spectroscopy (ICP-OES; Varian Visa-Pro; Agilent Technologies, Santa Clara, CA). To determine the crystal structure, we analyzed the powders by coupled θ–2θ XRD (D8 Advance; Bruker, Karlsruhe, Germany) with a CuK_α source (λ = 1.54056 Å) and electron diffraction in a TEM with a C_s-aberration-corrected probe (JEM-ARM 200CF; JEOL, Tokyo, Japan) at 200 keV. Using an EDXS (Centurio, JEOL) attached to the TEM, we also analyzed the local elemental distribution with nanoscale spatial resolution in STEM mode (probe size *ca.*2 Å, probe current *ca.* 700 pA, spectrum image collection time of 1458 s). We determined the phase composition by Rietveld refinement analysis of the XRD results. Specimen for electron microscopy analysis were prepared in two ways: (1) by focused ion beam milling of a lamella from a single particle and (2) by cold isostatic pressing of the powders into a pellet, which was then sintered at 1423 K in varigon (96% Ar/4% H_2) for 3 h; the pellet was sliced, so that the middle of the pellet could be mechanically thinned, then ion milled to 200 keV electron transparency.

We characterized the globally averaged optical properties of the powders at room temperature by measuring the photoluminescence emission (PL) using a HeCd laser source (λ_{ex} = 325 nm, 8 mW), an integrating sphere, and an Ocean Optics USB4000 spectrometer. Using a photomultiplier tube (H7421; Hamamatsu, Bridgewater, NJ) coupled with photon counting unit (C-8855, Hamamatsu), we measured the afterglow decay curves, after first sensitizing the powders with a UV source (λ_{ex} = 365 nm) for 10 min. Finally, we performed nanoscale spatially resolved cathodoluminescence (CL) under liquid nitrogen cooling in a dedicated scanning transmission electron microscope (STEM; VG HB501, Vacuum Generators, East Sussex, U.K.) at 60 keV with *ca.* 20 pA of beam current using a liquid N_2-cooled specimen and a custom-built CL system.[24] All CL spectra were calibrated in wavelength with a Hg spectrum acquired under the same experimental conditions.

III. Results

To investigate the effect of boron on structural evolution and equilibrium phase formation, we analyzed the Eu^{2+} and Dy^{3+} codoped $(SrO)_4{\cdot}(Al_2O_3)_7$ compounds by TG-DTA in air ambient (Fig. S1, Table S1), ICP-OES (Fig. S2, Table S2), and powder X-ray diffraction θ–2θ scans in ambient conditions. The TG-DTA and ICP-OES results are detailed in the Supporting Information, whereas diffractograms of samples with and without boron are summarized in Fig. 1. The boron-free samples contained a mixture of SA_6, SA_6, and S_4A_7 phases. However, when boron was incorporated into system, we observed that the S_4A_7 phase is clearly dominant, whereas a much smaller fraction of SA_2 phase can still be seen.

To determine the relative amount of each phase present, we performed Rietveld refinement analysis on the XRD data (see Fig. S3) and quantified the amount of each phase present. In the absence of boron, although the S_4A_7 phase fraction was dominant, the SA_2 phase was also present in substantial amounts. However, the boron-containing samples were composed predominantly of the S_4A_7 phase (see Fig. S4 and Table I).

To evaluate further the effect of boron on the luminescence properties of $Sr_4Al_{14}O_{25}:Eu^{2+},Dy^{3+}$ phosphors, we analyzed the photoluminescence emission spectra (see Fig. S5). Consistent with other reports in the literature, we observed two broad emission peaks, one located *ca.* 420 nm, and another *ca.* 490 nm. Such emission has been attributed

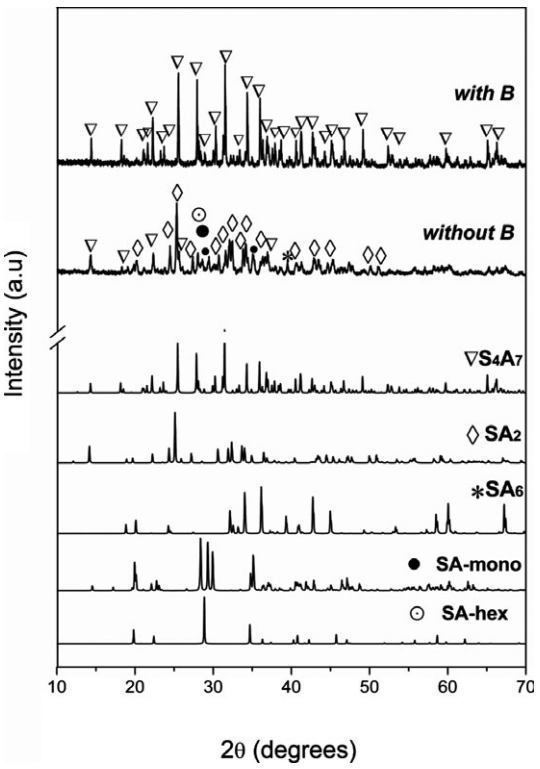

Fig. 1. X-ray diffractograms of boron-free and 4.3 at.% boron-doped SAEDB phosphors (2θ from 10 to 70° with 0.01° step size), obtained after TG-DTA analysis using a heating rate of 10°/min in air.

to $4f^6 5d^1$–$4f^7$ transitions in Eu^{2+} ions located at two crystallographically nonequivalent Sr^{2+} sites.[3,25,26] With increasing B content, emission at *ca.* 420 nm increased, whereas emission at *ca.* 490 nm decreased relatively.

To quantify the impact of boron in extending persistence, we measured the afterglow decay of the emission at 490 nm of the S_4A_7 phosphors under ambient conditions. S_4A_7 powders both with and without boron exhibited persistent luminescence The boron-containing samples luminesced for longer than 14 h, after being illuminated with a UV light source (365 nm) for 10 min, whereas, the persistence duration of the boron-free compounds lasted only a few minutes (Fig. S6). These decay characteristics are consistent with other work reported in the literature.[27] The PL emission spectra and the afterglow decay plots and details of the quantitative comparison are presented in the Supporting Information (Table S3).

To evaluate the effect of boron on the microstructural evolution of the doped S_4A_7 compounds, we conducted imaging and diffraction analysis in the TEM. Without B present, the SA particles consisted of aggregates of many grains, including some highly anisotropic, platelike grains that appear to have undergone abnormal grain growth (e.g., see Fig. 2, the grain labeled "1"). However, when B is present, such platelike grains were not present. Indexing the selected area diffraction pattern from the more equiaxed grains (the grains labeled "2" and "3" in Fig. 2) revealed that these were of the orthorhombic S_4A_7 phase, consistent with spot electron-diffraction patterns of boron-doped $Sr_4Al_{14}O_{25}$:Eu^{2+},Dy^{3+} (see Fig. S7).

Another way to investigate the distribution of the rare-earth dopants (RE), Eu and Dy, in the microstructure is nano-CL in a dedicated STEM, which enables the mapping of cathodoluminescence by rastering with a nanoscale probe in a dedicated STEM, that is, correlating nanoscale-localized microstructure with optical properties.[24] As Eu and Dy doped in SA compounds have characteristic radiative transitions in the visible spectrum, we analyzed spectrum images formed from the CL signals arising from these known $4f^6 5d$–$4f^7$ transitions of Eu^{2+} (*ca.* 420 and 490 nm) and $4f$–$4f$ transitions of Eu^{3+} and Dy^{3+}. Thus, the CL spectrum images enabled us to map not only the distribution of Eu atoms, but more specifically the distribution of Eu^{2+} and the trivalent

Table I. Phase Composition Revealed by Rietveld Analysis of the XRD Data from the S_4A_7ED Compounds with Boron Content as Determined by ICP-OES

Boron content (at.%)	S_4A_7 (wt%)	SA_6 (wt%)	SA_2 (wt%)	SA (wt%)
0	27.81	18.34	38.37	15.48
0.5	97.69	0	2.31	0
2	98.21	0	1.79	0
4.3	97.40	0	2.60	0

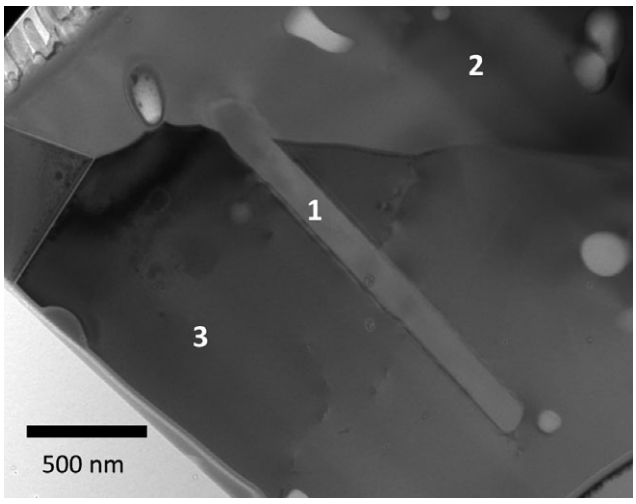

Fig. 2. Bright-field TEM image showing the polycrystalline microstructure of the boron-free S_4A_7ED compound: note the platelike grain 1, which is not present in B-doped specimen; the equiaxed S_4A_7 grains at points 2 and 3.

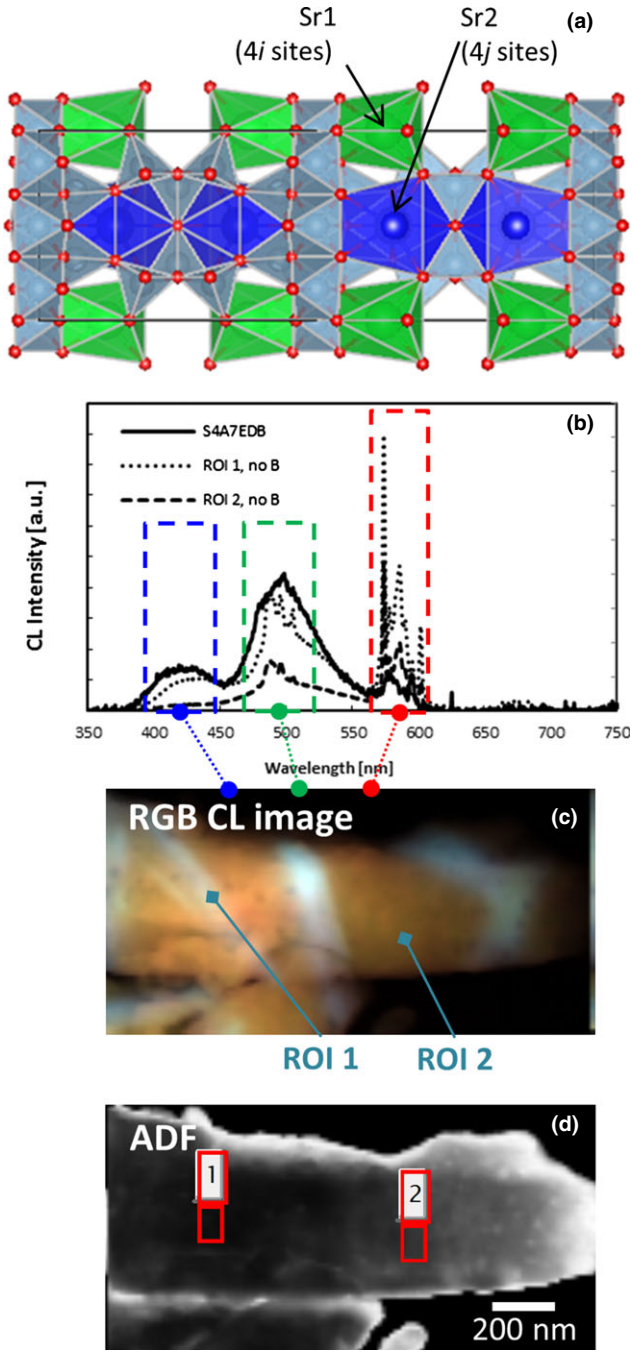

Fig. 3. (a) the crystal structure of $Sr_4Al_{14}O_{25}$: green = Sr^{2+} in 4*i* Wyckoff sites (Sr1), blue = Sr^{2+} in 4*j* Wyckoff sites (Sr2), gray = Al^{3+}, red = O^{2-}; (b) cathodoluminescence (CL) emission spectra from both boron-doped and boron-free S_4A_7EDB specimen (from 2 different regions analyzed); at *ca.* 420 nm, emission from Eu^{2+} in the Sr2 sites (i.e., the Sr^{2+} sites in blue); at *ca.* 490 nm, emission: from Eu^{2+} in the Sr1 sites (*i.e.* the Sr^{2+} sites in green)[35]; Region 1 a platelike grain; Region 2 equiaxed SA particles; (c) RGB image formed from CL emission from the spectral regions indicated: blue from 399 to 454 nm, green from 473 to 522 nm and red from 563 to 604 nm; (d) corresponding annular dark field image of the entire region analyzed by CL spectrum imaging.

RE ions, and even more specifically to discriminate between Eu^{2+} ions occupying the two different types of sites in the Sr^{2+} sublattice of $Sr_4Al_{14}O_{25}$ [as shown in Fig. 3(a)].[2,7,26]

The specimen containing 4.3 at.% B, a single crystal of S_4A_7, showed two broad emission bands in the CL spectrum at ca. 420 and 490 nm [Fig. 3(b), solid line]. Both are consistent with $4f^65d$–$4f^7$ radiative relaxation in Eu^{2+}, when exposed to two different crystal field potentials. This situation has been reported for Eu^{2+}, when occupying two crystallographically nonequivalent Sr^{2+} sites in S_4A_7. The radiative relaxation corresponding to emission at *ca.* 420 nm is associated with Eu^{2+} occupying an Sr2 site (i.e., the 4*j* Wyckoff sites), whereas the emission at *ca.* 490 nm originates from Eu^{2+} in an Sr1 site (i.e., the 4*i* Wyckoff sites).[2,26–28] An additional emission band is also present at ca. 580 nm, and may be ascribed to the $^4F_{9/2}$–$^6H_{13/2}$ transitions of Dy^{3+}; to distinguish between the 2 RE contributions, we note that the dominant transition of Eu^{3+} occurs at *ca.* 615 nm,[29] and the $^4F_{9/2}$–$^6H_{11/2}$ transition of Dy^{3+} appears at ca. 575 nm.[30] Since features of weak intensity can be observed at *ca.* 602 nm and at ca. 673 nm, we attribute the emission in the 575–580 nm range to Dy^{3+}. It should be noted that the lamella was produced by FIB thinning from a single crystal particle of S_4A_7 phase [as determined from the indexed diffraction pattern in Fig. S7(a)] and that the CL spectrum is relatively uniform across the entire specimen of thickness ~113 nm.

In addition to the CL spectrum representative of the boron-doped compound, two characteristic spectra are also shown in Fig. 3(b) from a boron-free specimen. One type of CL emission arises from the platelike grains [the dotted line in Fig. 3(b)], whereas the other is produced from the more equiaxed grains [the dashed line in Fig. 3(b)]. The CL emission from Eu^{2+} appeared to be largely confined to the crystals of platy habit, where emission from *ca.* 420 and 490 nm was strong. CL emission from these transitions was much weaker from the surrounding material. On the other hand emission from *ca.* 585 nm appeared more uniformly across the entire microstructure analyzed. Emission in this region is consistent with primarily that from 4*f* to 4*f* transitions in Dy^{3+}, albeit with a lesser amount of Eu^{3+}.[29] We conclude that the distribution of trivalent RE ions is uniform across the microstructure.

Although seldom observed in room-temperature PL studies of phosphor powders,[31,32] due to the relatively lower probability of parity-forbidden $4f \rightarrow 4f$ transitions in trivalent Eu and Dy, the nano-CL system has higher energy resolution and detection sensitivity at 100K, enabling detection of these transitions, even in the presence of dominant emission from Eu^{2+}. With the nano-CL system, to collect sufficient signal from the FIB lamella of the B-doped specimen, it was necessary to use a lower energy resolution in the optical detection system. Despite this concession, substantial emission *ca.* 585 nm was still detected [Fig. 3(b), solid line]. However, the relatively thicker B-free specimen luminesced more strongly, enabling use of the optics in a higher energy resolution configuration. Hence, the spectra obtained in the nano-CL system may reveal substantially more information, due to the capability for resolving the sharp, weaker emission in the red spectrum. Because CL analysis of minerals containing trivalent Eu or Dy have revealed the strongest characteristic transitions in the range 573–700 nm, detailed spectral decomposition studies will help resolve any contribution from trivalent Dy.[30]

By assigning the emission from *ca.* 420 nm to the blue channel, *ca.* 490 nm to green, and *ca.* 585 nm to red, a red-green-blue (RGB) image can be used to demonstrate the relative distribution of CL emission sources in the microstructure [see Fig. 3(c) and Fig. S8]. Regions that appear white in the RGB image reflect a mix of signals from the red channel, the green channel, and the blue channel with equal contribution. In contrast, the orange regions reflect a mixture of signals from the red channel predominantly, albeit with more limited contribution from the green one and none from the blue channel. Note that the polycrystalline nature of the specimen can be distinguished from the contrast in the annular dark-field (ADF) image in Fig. 3(d). Direct comparison between the ADF and the RGB images reveals that differences in the microstructure arise primarily from a nonuniform distribution of optically active emitters between grains.

To evaluate the stoichiometry of different regions of the microstructure shown in Fig. 2, we performed EDXS analysis. The results summarized in Fig. 4 (full spectrum shown in Fig. S9) were obtained from quantifying the spectra extracted from a spectrum image. The platelike grain, labeled as ROI #1, contained an Al:Sr at.% ratio of 8 and an enrichment in Eu. The surrounding equiaxed grains, represented by the spectrum from ROI #2, had an Al:Sr at.% ratio of 2.3, and the Eu and Dy content was generally below the sensitivity limit of EDXS. Further analysis of the microstructure from other regions of a B-free specimen far away from the platelike grain revealed an Al:Sr ratio *ca.* 2.3 and with a Eu content ranging 0.19–0.38 at.% and a Dy content ranging 0–0.23 at.%.

In the 4.3 at.% B-doped specimen, EDXS analysis revealed a uniform Al:Sr at.% ratio of *ca.* 2.3 and a uniform Eu and Dy content of 0.64 and 0.21 at.%, respectively, consistent with the results of nano-CL.

IV. Discussion

To assess the effect of boron on dramatically extending the afterglow in $Sr_4Al_{14}O_{25}$:Eu^{2+},Dy^{3+}, we considered its impact on the microstructure, the composition, and the luminescence properties. Combining the results of thermal analysis, XRD,

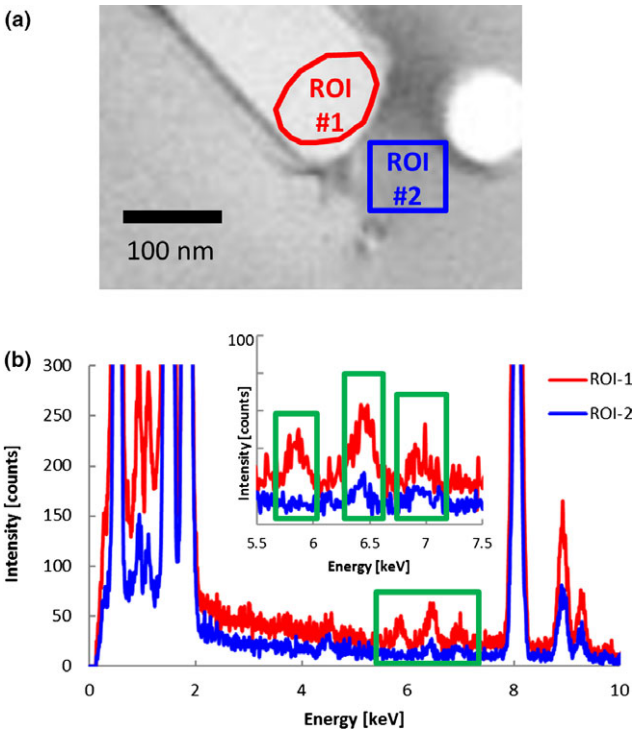

Fig. 4. (a) Bright-field TEM image of a boron-free S4A7ED specimen (zoomed in view, from Fig. 2), with the two regions analyzed by EDXS indicated and b) the corresponding EDXS spectra; ROI #1 of the platelike grain, ROI #2 of the neighboring equiaxed grain; Al-K at 1.49 keV and Sr-L at 1.58 keV were used for quantifying the Al:Sr ratio. Inset: Peaks for Eu-L_α at 5.85 keV, Eu-L_β at 6.46 keV, Dy-L_α at 6.49 keV and Eu-$L_{\beta 2}$ at 6.84 keV revealed that Eu and Dy were predominantly concentrated in the platelike grain. Both Eu and Dy were below the sensitivity limit in ROI #2. Corresponding full spectrum in Fig. S9.

and imaging and diffraction analysis in the electron microscope, we confirm that boron facilitates the microstructural evolution of the equilibrium S_4A_7 crystalline grains in ceramic powders prepared from a nominal $Sr_4Al_{14}O_{25}$ stoichiometry. Thermal analysis revealed that the onset temperature of crystallization from the amorphous precursor decreased with increasing boron content up to 4.3 at.%. XRD analysis of the products of TG-DTA revealed that the boron-free compounds consisted of multiple SA phases—that is, SA, SA_2, S_4A_7, SA_6—, whereas boron-doped compounds were dominated by the formation of S_4A_7 with increasing boron content, with the 4.3 at.% B compound becoming 97.40 wt% S_4A_7 and 2.6 wt% SA_2. These results are consistent with existing work in the literature, and validate the role of B as a sintering aid.[33]

ADF-STEM images revealed substantial differences in the microstructure, particularly when comparing that between boron-free and the 4.3 at.% boron-doped compounds. The boron-free powders contained some platelike, anisotropic grains of unusually high aspect ratio, in addition to neighboring equiaxed crystals of *ca.* 10 μm in diameter. In contrast, the 4.3 at.% boron-doped powders contained many large (*ca.* 20 μm diameter), equiaxed crystal grains of S_4A_7 phase. These results further substantiate that boron is necessary to stabilize the formation of the S_4A_7 phase.[7,27] In fact, our results suggest that many of the phases present in the equilibrium $SrO\text{-}Al_2O_3$ binary system are metastable and are able to form due to favorable local kinetics in the dried amorphous gel. However, the presence of boron, by lowering viscosity in the amorphous precursor, appeared to have substantially lowered the formation energy of the equilibrium phase, S_4A_7, enabling a strong preference for that phase to form in the evolving microstructure, at the expense of the other SA phases: SA_6, SA, SA_2, *etc.*

Comparing the compositional variations between boron-free and 4.3 at.% boron-doped S_4A_7 compounds revealed additional insight into the substantial impact of boron. Using STEM-EDX, we observed two types of compositional variations. If the region analyzed was contained in a platelike grain, the composition was Al-rich (Al:Sr cation ratio of 8) and contained a much higher Eu content, with an inconclusive Dy content, whereas the surrounding equiaxed grains did not contain enough Eu to be above the detectability limit. In the absence of these anisotropic grains, the Al:Sr cation ratio was more uniform, ranging from 1.5 to 3.1, and a corresponding Eu content spanning 0.38–0.19 at.%. In the B-doped S_4A_7 specimen, the TEM lamella was a single crystal with a uniform distribution of Eu. Although the Al:Sr cation ratio should theoretically be 3.5 (from 14 Al cations per 4 Sr cations per mole of $Sr_4Al_{14}O_{25}$), a cation ratio value of 2.3 was determined from EDX measurements on regions, whose SADP's had indexed to S_4A_7. Thus, we consider 2.3 to be the reference value for S_4A_7.

In the boron-free compounds, the trivalent RE ions were present throughout the microstructure, whereas Eu^{2+} appeared primarily in the Sr1 sites (i.e., in the higher symmetry 4*i* Wyckoff sites). Only in the platelike grains, would emission arise from the Eu^{2+} in Sr2 sites (i.e., in the lower symmetry 4*j* Wyckoff sites). In contrast, in the B-doped large single crystal, Eu^{2+} is uniformly present in both types of Sr sites, in addition to a homogeneous signal from both Dy^{3+} and Eu^{3+}. It should be noted that when using PL, the Eu^{3+} was not detectable, possibly because its emission was below the detector sensitivity limit. These results are summarized in Table II.

Combining this evidence for the effect of B on microstructure, composition, and luminescence in Eu and Dy codoped S_4A_7 compounds, we report an association between long afterglow persistence and a uniform distribution of Eu^{2+} in Sr2 sites. When B is present, S_4A_7 is the equilibrium phase and dominates the microstructure; the composition and distribution of optically active ions are uniform; and the afterglow persists for longer than 14 h. However, without B doping, in an SA compound of the same nominal S_4A_7 stoichiometry, there is a broader range of homogeneity in cation stoichiometry in the microstructure, as well as persistence abbreviated to *ca.* 10 min. The localized stoichiometric variation gives rise to the formation of crystalline grains of a variety of SA phase. Nano-CL shows that the distribution of trivalent RE ions is homogenous, but Eu^{2+} is localized to the anisotropic grain and absent from the neighboring equiaxed grains. It should also be noted that even though there is a high content of Eu^{2+} in Sr2 sites in B-free, Al-rich, anisotropic grains, the short afterglow may possibly be evidence of concentration quenching.[12]

Table II. Summary of CL Spectrum Characteristics and the Corresponding Origin of Transitions

Region analyzed	Eu^{2+} in 4*j* sites (*ca.* 420 nm)	Eu^{2+} in 4*i* sites (*ca.* 490 nm)	Dy^{3+} (*ca.* 580 nm)
B-free, platy	Strong	Strong	Present
B-free, equiaxed	Weak	Weak	Present
4.3 at.% B-doped	Strong	Strong	Present

Previous investigations correlating luminescence behavior with Al:Sr ratio (in B-free samples) were performed on pressed powder pellets 10 mm in diameter and 5 mm in thickness.[34] Emission was evaluated from many particles, and it was assumed that 2 phases, SA and SA_6, were the only ones present. However, electron diffraction and spatially resolved elemental spectroscopy from individual grains now reveal that at the local scale, there is a much more complicated microstructure and elemental distribution in B-free SA phosphor powders. With a broader range of cation stoichiometry, the consequent increased diversity in crystal field environments of Eu^{2+} results in a richer range of transitions arising from more variation in energy level separation, accounting for the broad bandwidth at *ca.* 420 and 490 nm.

Our results are also consistent with the observations reported by Chen et al.—the addition of boron enhanced both the initial afterglow intensity and the persistence intensity over time in Eu and Dy codoped SA.[12] After all, higher emission intensity would be associated with increased Eu^{2+} concentration in the crystal structure. Without boron, less Eu^{2+} would be incorporated into the SA crystal structure, whereas with B present, the Eu^{2+} content is higher and more uniformly distributed at the nanoscale.

IV. Conclusions

By combining insights obtained from thermal analysis, XRD, PL, EDS, and nano-CL in a STEM, we report evidence suggesting that boron improves the homogeneous distribution of optically active Eu^{2+} into 4*j* Wyckoff site in the Sr^{2+} sublattice, which is necessary for persistence longer than 14 h in B, Eu^{2+} and Dy^{3+} codoped $Sr_4Al_{14}O_{25}$ phosphors. The presence of B facilitates the evolution of a microstructural morphology consisting of large, equiaxed single-phase grains, with a uniform distribution of trivalent RE and Eu^{2+} ions. However, the absence of B allows the formation of multiple phases of $SrO\text{-}Al_2O_3$, including high aspect ratio, Al-rich and Eu-rich grains, surrounded by regions depleted in Eu and Dy content. Although overall the RE's appear as trivalent ions uniformly throughout this microstructure, the distribution of optically active Eu^{2+} depends on the local Sr site coordination, of which there are two in the S_4A_7 phase. Eu^{2+} ions occupying the higher symmetry 4*i* Wyckoff site of Sr were distributed uniformly. However, Eu^{2+} appeared in the lower symmetry 4*j* Wyckoff site of Sr only in the platelike grains. Thus, based on maps of cathodoluminescence at nanoscale resolution, we conclude that a necessary condition for extended afterglow in S_4A_7ED is the homogeneous distribution of Eu^{2+} in the microstructure.

Acknowledgment

The authors gratefully acknowledge Attila Yazici for ICP-OES measurements, Medeja Gec for TEM specimen preparation of the sintered pellet, and Meltem Sezen for fruitful discussions on FIB specimen preparation. Funding from project #212T177 and #112M360 is acknowledged from the Scientific and Technological Research Council of Turkey (TÜBİTAK). The research leading to these results has received funding from the European Union Seventh Framework Programme [No. FP7/2007-2013] under Grant Agreement No. n312483 (ESTEEM2).

Supporting Information

Additional Supporting Information may be found in the online version of this article:

Data S1. Supplementary Information.

References

[1]F. C. Palilla, A. K. Levine, and M. R. Tomkus, "Fluorescent Properties of Alkaline Earth Aluminates of the Type MAl_2O_4 Activated by Divalent Europium," *J. Electrochem. Soc.*, **115** [6] 642–4 (1968).

[2]B. Smets, J. Rutten, G. Hoeks, and J. Verlijsdonk, "$2SrO \cdot 3Al_2O_3 : Eu^{2+}$ and 1.29(Ba, Ca)O,$6Al_2O_3$:Eu^{2+}: Two New Blue-Emitting Phosphors," *J. Electrochem. Soc.*, **136** [7] 2119–23 (1989).

[3]Y. Lin, Z. Tang, and Z. Zhang, "Preparation of Long-Afterglow $Sr_4Al_{14}O_{25}$-Based Luminescent Material and Its Optical Properties," *Mater. Lett.*, **51** [1] 14–8 (2001).

[4]T. Nakamura, et al., "High Frequency EPR Investigations of Gadolinium (III)-Doped Strontium Aluminates," *Phys. Chem. Chem. Phys.*, **3** [9] 1721–3 (2001).

[5]F. Clabau, et al., "Mechanism of Phosphorescence Appropriate for the Long-Lasting Phosphors Eu^{2+}-Doped $SrAl_2O_4$ with Codopants Dy^{3+} and B^{3+}," *Chem. Mater.*, **17** [15] 3904–12 (2005).

[6]D. Wang, Y. Li, Q. Yin, and M. Wang, "Concentration Quenching of Eu^{2+} in $4SrO{\cdot}7Al_2O_3$:Eu^{2+} Phosphor," *J. Electrochem. Soc.*, **152** [1] H15–8 (2005).

[7]J. T. C. Van Kemenade and G. P. F. Hoeks, "New (Eu-Activated) Barium and Strontium Aluminates with Very Efficient Eu^{2+} Luminescence"; pp. 914–5 in Electrochemical Society Spring Meeting 1983 Extended Abstracts, San Francisco, May 8-13, 1983, (Abstract 607).

[8]S. H. M. Poort and G. Blasse, "The Influence of the Host Lattice on the Luminescence of Divalent Europium," *J. Lumin.*, **72–74**, 247–9 (1997).

[9]M. Nazarov, M. G. Brik, D. Spassky, B. Tsukerblat, A. Nor Nazida, and M. N. Ahmad-Fauzi, "Structural and Electronic Properties of $SrAl_2O_4$:Eu^{2+} from Density Functional Theory Calculations," *J. Alloys Compd*, **573**, 6–10 (2013).

[10]T. Matsuzawa, Y. Aoki, N. Takeuchi, and Y. Murayama, "A New Long Phosphorescent Phosphor with High Brightness, $SrAl_2O_4$:Eu^{2+}, Dy^{3+}," *J. Electrochem. Soc.*, **143** [8] 2670–3 (1996).

[11]T. Aitasalo, J. Holsa, H. Jungner, M. Lastusaari, and J. Niittykoski, "Mechanisms of Persistent Luminescence in Eu^{2+}, RE^{3+} Doped Alkaline Earth Aluminates," *J. Lumin.*, **94**, 59–63 (2001).

[12]I.-C. Chen and T.-M. Chen, "Sol–Gel Synthesis and the Effect of Boron Addition on the Phosphorescent Properties of $SrAl_2O_4$:Eu^{2+},Dy^{3+} Phosphors," *J. Mater. Res.*, **16** [3] 644–51 (2001).

[13]A. Nag and T. R. N. Kutty, "Role of B_2O_3 on the Phase Stability and Long Phosphorescence of $SrAl_2O_4$:Eu, Dy," *J. Alloys Compd*, **354** [1–2] 221–31 (2003).

[14]J. Niittykoski, et al., "Effect of Boron Substitution on the Preparation and Luminescence of Eu^{2+} Doped Strontium Aluminates," *J. Alloys Compd*, **374** [1–2] 108–11 (2004).

[15]F. Clabau, X. Rocquefelte, T. Le Mercier, P. Deniard, S. Jobic, and M.-H. Whangbo, "Formulation of Phosphorescence Mechanisms in Inorganic Solids Based on a New Model of Defect Conglomeration," *Chem. Mater.*, **18** [14] 3212–20 (2006).

[16]J. Hölsä, T. Laamanen, M. Lastusaari, J. Niittykoski, and P. Novák, "Electronic Structure of the $SrAl_2O_4$:Eu^{2+} Persistent Luminescence Material," *J Rare Earth*, **27** [4] 550–4 (2009).

[17]M. Buijs, A. Meyerink, and G. Blasse, "Energy Transfer Between Eu^{3+} Ions in a Lattice with Two Different Crystallographic Sites: Y_2O_3:Eu^{3+}, Gd_2O_3:Eu^{3+} and Eu_2O_3," *J. Lumin.*, **37**, 9–20 (1987).

[18]T. Aitasalo, et al., "Persistent Luminescence Phenomena in Materials Doped with Rare Earth Ions," *J. Solid State Chem.*, **171** [1–2] 114–22 (2003).

[19]G. Blasse, "Energy Transfer Between Inequivalent Eu^{2+} Ions," *J. Solid State Chem.*, **62** [2] 207–11 (1986).

[20]E. Nakazawa and T. Mochida, "Traps in $SrAl_2O_4$:Eu^{2+} Phosphor with Rare-Earth Ion Doping," *J. Lumin.*, **72–74**, 236–7 (1997).

[21]E. Nakazawa, Y. Murazaki, and S. Saito, "Mechanism of the Persistent Phosphorescence in $Sr_4Al_{14}O_{25}$:Eu and $SrAl_2O_4$:Eu Co-Doped with Rare Earth Ions," *J. Appl. Phys.*, **100** [11] 113113, 7pp (2006).

[22]M. G. Eskin, "The Role of Boron in Phosphorescence Persistence of Rare-Earth Co-Activated Alkalai Aluminates"; M.Sc. Thesis, Sabanci University, Istanbul, Turkey, August 2011.

[23]G. Inan Akmehmet, "Investigating the Origins of Long Persistence in Strontium Aluminate Phosphors by Nanoscale Resolved Imaging and Spectroscopy"; Ph.D. Thesis, Sabanci University, Istanbul, Turkey, August 2015.

[24]L. F. Zagonel, et al., "Nanometer Scale Spectral Imaging of Quantum Emitters in Nanowires and Its Correlation to Their Atomically Resolved Structure," *Nano Lett.*, **11** [2] 568–73 (2011).

[25]C. K. Chang, L. Jiang, D. L. Mao, and C. L. Feng, "Photoluminescence of $4SrO{\cdot}7Al_2O_3$ Ceramics Sintered with the Aid of B_2O_3," *Ceram. Int.*, **30** [2] 285–90 (2004).

[26]D. Dutczak, T. Jüstel, C. Ronda, and A. Meijerink, "Eu^{2+} Luminescence in Strontium Aluminates," *Phys. Chem. Chem. Phys.*, **17**, 15236–49 (2015).

[27]A. Nag and T. R. N. Kutty, "The Mechanism of Long Phosphorescence of $SrAl_{2-x}B_xO_4$ ($0 < x < 0.2$) and $Sr_4Al_{14-x}B_xO_{25}$ ($0.1 < x < 0.4$) Co-Doped with Eu^{2+} and Dy^{3+}," *Mater. Res. Bull.*, **39**, 331–42 (2004).

[28]J. Hölsä, T. Aitasalo, H. Jungner, M. Lastusaari, J. Niittykoski, and G. Spano, "Role of Defect States in Persistent Luminescence Materials," *J. Alloys Compd*, **374** [1–2] 56–9 (2004).

[29]V. Abbruscato, "Optical and Electrical Properties of $SrAl_2O_4$:Eu^{2+}," *J. Electrochem. Soc.*, **118** [6] 930–2 (1971).

[30]P. Blanc, A. Baumer, F. Cesbron, D. Ohnenstetter, G. Panczer, and G. Remond, "Systematic Cathodoluminescence Spectral Analysis of Synthetic Doped Minerals: Anhydrite, Apatite, Calcite, Fluorite, Scheelite and Zircon"; pp. 127–60 Chapter 5 in *Cathodoluminescence in the Geosciences*, 3rd edition, Edited by M. Pagel, V. Barbin, P. Blanc, and D. Ohnenstetter. Springer, Heidelberg, 2013.

[31]W. Jia, H. Yuan, L. Lu, H. Liu, and W. M. Yen, "Phosphorescent Dynamics in $SrAl_2O_4$:Eu^{2+},Dy^{3+} Single Crystal Fibers," *J. Lumin.*, **76–77**, 424–8 (1998).

[32]M. Kamada, J. Murakami, and N. Ohno, "Excitation Spectra of a Long-Persistent Phosphor $SrAl_2O_4$: Eu, Dy in Vacuum Ultraviolet Region," *J. Lumin.*, **87–89**, 1042–4 (2000).

[33]Y.-M. Chiang, D. P. Birnie, and W. D. Kingery, *Physical Ceramics*, pp. 392–420. John Wiley&Sons, New York, NY, 1997.

[34]I.-C. Chen and T.-M. Chen, "Effect of Host Compositions on the Afterglow Properties of Phosphorescent Strontium Aluminate Phosphors Derived from the Sol–Gel Method," *J. Mater. Res.*, **16** [5] 1293–300 (2001).

[35]K. Momma and F. Izumi, "VESTA 3 for Three-Dimensional Visualization of Crystal, Volumetric and Morphology Data," *J. Appl. Crystallogr.*, **44** [6] 1272–6 (2011). □